

Dynamical properties and acceleration of hierarchical dust in the vicinity of comet 67P/Churyumov–Gerasimenko

Yu. Skorov,^{1,2★} V. Reshetnyk,^{3,4★} L. Rezac,² Y. Zhao,⁵ R. Marschall,⁶ J. Blum¹ and P. Hartogh²

¹*Institut für Geophysik und extraterrestrische Physik, Technische Universität Braunschweig, Mendelssohnstr. 3, D-38106 Braunschweig, Germany*

²*Max-Planck-Institut für Sonnensystemforschung, Justus-von-Liebig-Weg 3, D-37077 Göttingen, Germany*

³*Taras Shevchenko National University of Kyiv, Glushkova ave. 2, 01601 Kyiv, Ukraine*

⁴*Main Astronomical Observatory of National Academy of Science of Ukraine, Akademika Zabolotnogo Str 27, UA-03680 Kyiv, Ukraine*

⁵*Key Laboratory of Planetary Sciences, Purple Mountain Observatory, Chinese Academy of Sciences, Nanjing, China*

⁶*International Space Science Institute, Hallerstrasse 6, CH-3012 Bern, Switzerland*

Accepted 2018 April 16. Received 2018 April 10; in original form 2018 January 3

ABSTRACT

A significant fraction of cometary dust grains leaving the nucleus surface are extremely porous and fluffy particles as revealed by recent observation from the Rosetta mission. In this paper our aim is to investigate the dynamics of such grains when subjected to a gas flow, representing the cometary outgassing. We perform numerical experiments to quantify how the internal porous texture is reflected in quantities such as effective cross-section, gas drag coefficient, and light scattering efficiency. We also derive particle speeds for the different types of aggregates as a function of radial distance and compare them to the observations by the GIADA instrument. Using our original method for constructing hierarchical aggregates we increase the level of aggregation to reach particle sizes up to few millimeters, consistent with the observations. In addition, a non-constant gas velocity is now considered in the framework of free molecular as well as fully collisional flow models, and radiation pressure calculations use the effective medium theory appropriate for such particles. These improvements lead us to conclude that dynamical models should account for accelerating gas flow, which leads to a smaller terminal speed of fluffy dust grains. Secondly, solar radiation pressure calculated based on the Mie theory approximation can lead to orders of magnitude error for the very porous particles, instead the effective medium theory should be used. Finally, although numerical simulations can reproduce the GIADA measurements of dust speeds, we cannot conclude that there exists a preferred model of porous particles build as a ballistic cluster aggregate.

Key words: methods: numerical – comets: general – comets: individual:67P/Churyumov–Gerasimenko.

1 INTRODUCTION

This paper is a continuation of the work initiated by Skorov et al. (2016), hereafter referred to as [Paper I](#), investigating forces acting on cometary dust particles in the vicinity of the nucleus. In [Paper I](#), we introduced a new model capable of simulating large and porous dust particles constructed by hierarchical agglomeration. These investigations are necessary to accurately determine the dynamical properties (i.e. effective cross-section and ratio of cross-section to mass) for the non-spherical and highly porous agglomerates observed by the Rosetta instruments (Rotundi et al. 2015; Fulle et al. 2015, 2016; Langevin et al. 2016; Bentley et al. 2016; Ott et al.

2017). For a detailed description of motivation, observed cometary dust properties from 67P/C-G, and the state-of-the-art of modelling we refer the reader to [Paper I](#). In the following summary, we present only the most important points of the quantitative analysis and the limiting assumptions of the earlier model. The model in [Paper I](#) could not reproduce the reported dust speeds except for conditions at about 3 au from the Sun, and could not match the weak correlation seen between the dust mass and the velocity. These results were attributed to the simplifying assumptions in the modelling of the gas flow field. In addition, the radiation pressure was calculated from the classical Mie theory, and we also note that only two hierarchic levels of aggregation were considered (with effective radius noticeably smaller than measured by GIADA Della Corte et al. 2015).

* E-mail: skorov@gmail.com (YS); reshetnyk@gmail.com (VR)

The purpose of this paper is to reduce these model simplifications and replace them with more realistic ones. In particular we (1) consider larger particles with masses up to a few milligrams, (2) apply gas expansion models based on the continuous (Euler) gas dynamics as well as for the free molecular flow (FMF), and (3) calculate radiation pressure based on the effective medium theory (EMT) appropriate for the high porosity particles (Shen, Draine & Johnson 2008). A more complete description of the model improvements is presented below. In Section 1, the dynamical properties of the model agglomerates is described and in Section 2 the new model block for calculations of the light pressure and the gas drag force is presented. In Section 3, we re-analyse the major forces acting on dust particles near the nucleus and estimate their importance in the context of 67P/C-G. Section 4 contains descriptions of the new results in the framework of the updated model, and in Section 5 we compare them to the first results obtained by instruments on-board Rosetta. Finally, we summarize this work in Section 6.

2 DYNAMICAL PROPERTIES OF HIERARCHICAL AGGREGATES

2.1 Model for aggregation

In Paper I, we described in detail the method for generating ballistic random porous aggregates. Both the classical approach of cluster growth [ballistic particle–cluster aggregates, BPCA, and ballistic cluster–cluster aggregates, BCCA, see Kozasa, Blum & Mukai (1992)] as well as ballistic aggregation with monomer migration (BAM) after collision (Shen et al. 2008) are considered. Following Shen et al. (2008), we examined three subclasses of ballistic aggregates (BA). The classical BA with hit-and-stick behaviour (BPCA) results in the most porous aggregates. BAM1 and BAM2 allow for one and two migrations, respectively, and produce aggregates of higher effective density. For instance, for a large number of monomers, N , the BPCA clusters have a filling factor (fraction of volume taken up by monomers) of about 0.15, whereas the BAM2 clusters have filling factors of about 0.30, i.e. twice the effective density. We note that all three resulting variants (BPCA, BAM1, and BAM2) have fractal dimensions of $D_f = 3$.

The hierarchical agglomeration is similar to the procedure used in application for protoplanetary dust for building the classical cluster–cluster aggregates (CCA) (Kozasa, Blum & Mukai 1992; Dominik et al. 2009; Okuzumi, Tanaka & Sakagami 2009). However, in the standard CCA model a pair of aggregates of the same mass collides at each simulation step, whereas in a hierarchical agglomeration model the target–aggregate is bombarded by pseudo-monomers that are aggregates of a lower level of organization. That is, each model’s pseudo-monomer is an aggregate constructed at the previous step of simulation. The first level is built from solid spherical monomers, the second level aggregates are built from first-level aggregates (considered as pseudo-monomers at this stage), and at the third level, the role of pseudo-monomers is then taken by the second-level of aggregates. For notation purposes, we will indicate the aggregation level as superscript. In this work, we examine mainly the third level of hierarchical aggregates (BA^3 , $BAM1^3$, and $BAM2^3$) and analyse their dynamical properties. We also note that similar to Paper I, the aggregate type does not change when going to a higher level, and all pseudo-monomers have the same size. These restrictions are not fundamental and can be removed if the physical reasons appear in the future.

When building the model dust particles, several physical considerations need to be taken into account. The size and density of the

monomers (used for the first level aggregates) has to be set, as well as the final size of the hierarchical aggregate after the third stage of aggregation. Our numerical simulations in the context of 67P/C-G rely on several Rosetta results. These indicate that the nucleus ejects porous particles from ten microns to few millimeters in size (Rotundi et al. 2015; Schulz et al. 2015). The COSIMA (Merouane et al. 2016) and MIDAS (Bentley et al. 2016; Mannel et al. 2016) instruments also found porous and lumpy structured dust particles at different scales, which further supports the hypothesis of hierarchical agglomeration. The bulk density of solid material (first stage monomers) is assumed to be 3500 kg m^{-3} (Li & Draine 2001).¹ As in Paper I, for a given number of monomers N , we generate 5 random aggregates of each type in order to statistically improve the reliability of the model.

2.2 Dynamical properties of aggregates

The effective cross-section of the aggregates, A , is estimated using Monte Carlo method. For a given number of monomers N , 15 variants (five aggregate implementations multiplied by three orthogonal projections) are used to estimate the average cross-section for a specific type and size of aggregate. In Fig. 1, we show the ratio of average aggregate cross-section A to the cross-section of a solid sphere A_{sphere} of the same mass. The value R_{eff} shown on the abscissa is defined here as the radius of a circle with an area equal to the average aggregate cross-section (Nakamura, Kitada & Mukai 1994). There are few other ways of defining this quantity, but they give rather similar results, the difference is a few per cent for $N > 2^{10}$ (see table 1 in Shen et al. 2008).

The largest aggregates contain 2^{36} (or about one hundred billion) monomers and have masses of about one milligram. The ratio A/A_{sphere} varies between 12 (the size of the corresponding $BAM2^3$ is about 2 mm) and 72 (the size of the corresponding BA^3 is about 3 mm). For the smaller aggregates ($N = 2^{12}$) of the second level, this ratio varies from 2 to 4 (see Paper I). It should be noted that for a given number of monomers (or equivalently, the mass of the aggregate) the geometrical properties of the hierarchical aggregates vary significantly. This is easily understood, because we can construct the same aggregate mass from either a large number of small pseudo-monomers or a small number of large pseudo-monomers. For example, the $100 \mu\text{m } BA^3$ changes the ratio A/A_{sphere} by a factor of two.

An important fact is that with increasing number of aggregation levels the particles become more loose and their characteristics are more markedly different from the compact sphere of the same mass. These results are demonstrated in Fig. 2, showing the ratio of cross-section A to the total cross-section of all constituent monomers $N \cdot A_m$. This value may characterize the degree of compactness of an aggregate (i.e. the degree of internal shadowing). For the open very fluffy BCCA, which have fractal dimension $D_f \sim 2$ (Kozasa et al. 1992) the shadowing effect is small: for the large, millimeter-sized aggregates, about 40 per cent of the total cross-section of monomers is still visible (Minato et al. 2006). In contrast, the large BA^3 and $BAM2^3$ aggregates exhibit a significant self-shadowing and less than 1 per cent of the total cross-section of all constituents is visible. The degree of shading for particles larger than one hundred microns grows approximately linearly with their size. It clearly shows that

¹For definiteness we consider only pure silicate grains. The latest results suggest a large amount of carbonaceous stuff with low bulk densities and different optical properties.

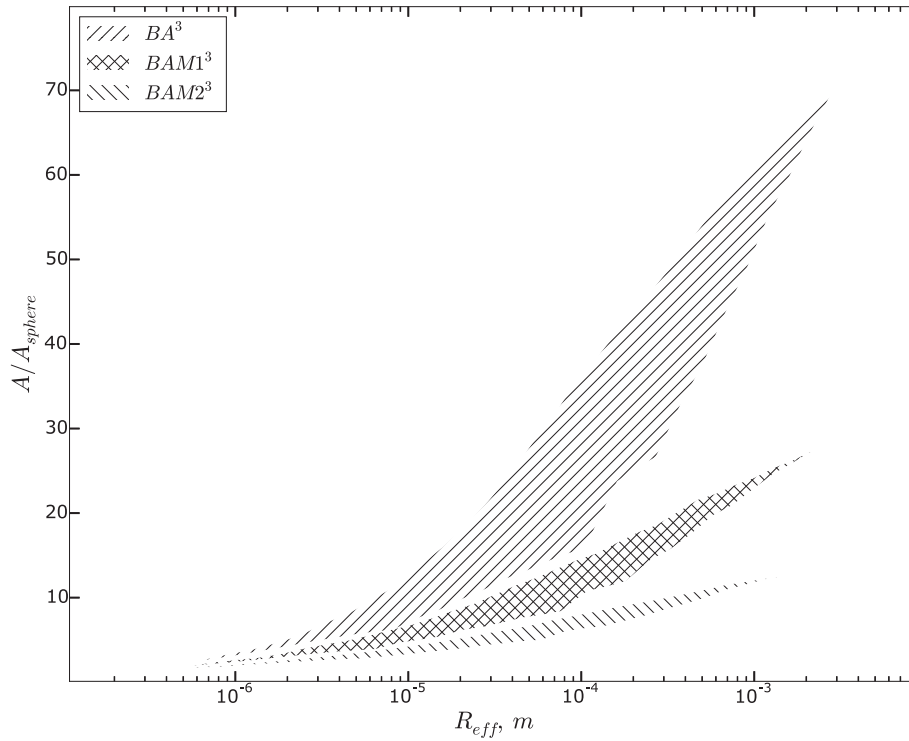


Figure 1. Ratio of aggregate cross-section, A , to cross-section of a sphere with equivalent mass, A_{sphere} , for hierarchic aggregates BA^3 , $BAM1^3$, and $BAM2^3$.

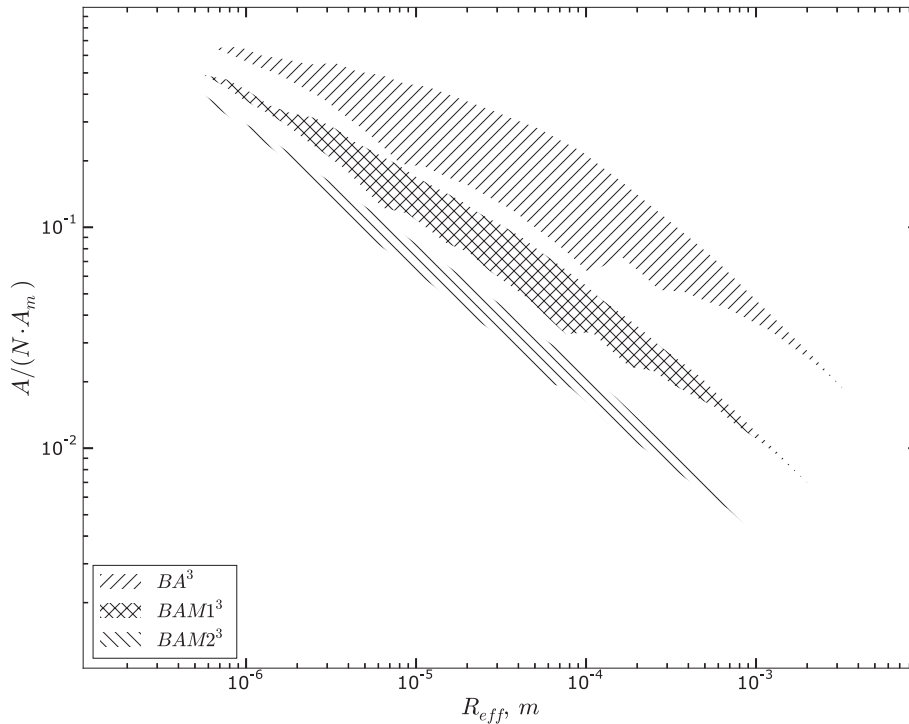


Figure 2. Shadowing effect for different types of hierarchic aggregates (BA^3 , $BAM1^3$, $BAM2^3$). Shown is the ratio of the aggregate cross-section, A , to total cross-section of all constituent monomers, $N \cdot A_m$, as a function of the effective aggregate radius.

our hierarchical aggregates have a fractal dimension of about 3 rather than 2, hence their dynamic properties are more similar to the properties of particle–cluster aggregates.

Next, we discuss estimates of porosity (or filling factor) and effective density of the aggregates. The filling factor is defined as $\Phi = V/V_{\text{eff}}$, where V is the total volume of the solid material in the particle and V_{eff} is the characteristic volume of the aggregate

calculated from R_{eff} . The filling factor Φ of hierarchical aggregates of levels 2 and 3 as a function of monomer number N is shown in Fig. 3. Φ is generally inversely proportional to N . Therefore, when N is about 10^{10} the filling factor of the BAM2³ is about 3 per cent and in case of the most fluffy BA³ aggregates Φ is about 10 times less.

Systematic calculations show that hierarchical aggregates of the third level may take almost any possible value of the filling factor between the limits determined by the most dense (BAM2³) and the most loose (BA³) aggregates. Thus, there are no sharp boundaries between aggregates constructed in different ways (with or without migration after collision). This conclusion is illustrated in Fig. 4, where we plot the filling factor as a function of R_{eff} for a variety of aggregates of hierarchical level 3. Note that the reduction of variance in Φ towards the largest R_{eff} is a result of a decrease in the degree of freedom in constructing the blocks: the largest aggregate in our model can be constructed in a single way. For 100 micron-sized particles Φ varies from about 0.003 to 0.07. As the density of an aggregate is proportional to Φ , which means that this quantity may also vary more than 20 times for particles of the same size (100 μm in this case). For millimeter-sized particles, the effective density may vary from ~ 10 to $\sim 100 \text{ kg m}^{-3}$ for different types of agglomeration (see Table 1).

3 FORCES ACTING ON THE DUST PARTICLES NEAR THE NUCLEUS

A dust particle that lost all its contacts with the cometary surface is accelerated by the flow of gas typically generated by subliming ice. In addition to the gas drag force, the motion of the dust is affected by the gravity of the nucleus and the (solar) radiation pressure. Other forces (e.g. Coulomb force) are not considered in this work.

3.1 Gas drag force, F_{GD}

An earlier discussed limitation introduced in Paper I was the assumption that the gas outflow has a constant speed. On one hand, this model simplification reduces the problem of dust acceleration to the simplest form and the velocity can be calculated analytically. On the other hand, this is a crude idealization for the near nucleus conditions and does need a verification. Therefore, we examine two limiting cases for the outflow of a gas. Namely, when the outflow is described in the continuous limit (Euler flow, EF), and then also in the FMF approximation. The required analytical solutions for these cases under the assumption of stationary outflow from a spherical condensed phase into a vacuum are presented in Sone & Sugimoto (1993). We refer the reader to Section IV in this work. The variation of the basic model parameters with the distance is shown in Table 2.

Regardless of the approximation in which the gas flow is described, the dust component is collisionless, and the molecular mean free path is much larger than the dust size even at small heliocentric distances. In this case, the acceleration of each dust particle should be simulated individually and the gas drag force F_{GD} is described by equation (2) of Paper I:

$$F_{\text{GD}}(l) = \frac{1}{2} C_{\text{D}} A n_{\text{I}} m_{\text{H}_2\text{O}} (u_{\text{I}} - v_d)^2. \quad (1)$$

The drag force depends on the gas drag coefficient C_{D} (discussed in Paper I), the effective particle cross-section A (presented in the previous subsection), the gas density $n_{\text{I}} m_{\text{H}_2\text{O}}$, the gas velocity u_{I} , and the dust particle velocity v_d . It should be also noted that this standard formulation has two hidden assumptions. First, the possible

kinetic non-equilibrium character of the gas outflow is not taken into account, and second, the gas momentum transfer to the dust particle is only via elastic collisions, which eliminates the need to consider the dust temperature in the model. A more detailed discussion is presented in Paper I.

3.2 Radiation pressure, F_{R}

Several sophisticated methods can be used to calculate the radiation pressure acting on a porous irregular particle. We refer the reader to the discussion in the corresponding section of Paper I. In general, the radiation pressure force (due to solar photons), F_{R} , acting on a dust particle of effective cross-section A at heliocentric distance R is given by:

$$F_{\text{R}} = \left(\frac{A}{c}\right) \left(\frac{R_0}{R}\right)^2 \int_0^\infty B_0(\lambda) Q_{\text{PR}}(m^*, \lambda) d\lambda, \quad (2)$$

where c is the speed of light, R_0 the solar radius, B_0 the radiance of the sun at wavelength λ , and Q_{PR} the radiation pressure efficiency coefficient, which depends on λ and on the refractive index m^* of the dust particle.

In Paper I, an approach outlined in Mukai et al. (1992) was used, where light pressure is calculated based on the geometrical cross-section A and the efficiency factor Q_{PR} , which is a function of grain size and composition. The classical Mie theory was used to calculate the scattering and absorption coefficients modelling Q_{PR} as a function of wavelength. The measured solar spectrum fluxes are taken from the National Renewable Energy Laboratory.²

The numerical calculations of Köhler et al. (2007) and Shen et al. (2008) clearly demonstrate a non-negligible dependence of scattering and absorption coefficients on the grain composition. Because cometary dust is expected to have a complex chemical makeup (Kissel et al. 1986; Schulz et al. 2015), this will also likely be the main source of uncertainty in calculating the optical properties of the dust. Recently Fulle et al. (2017), suggested about 22 ± 2 per cent of silicates in the observed 67P/C-G dust. Investigating an accurate determination of effective refractive index from first principles is beyond the scope of this paper, and in this work we apply the refractive index m^* (for silica grains) published by Laor & Draine (1993).

In this work we focus on improving the accuracy of calculations for the optical characteristics of dust aggregates of the third level (i.e. the largest particles). A combination of Mie theory and the EMT is used for that purpose. Because of the generally low value of the filling factor, the Maxwell–Garnett mixing rule (Bohren & Huffman 1983; Mukai et al. 1992) is applied in the model. This analysis showed that the effective dielectric constant, calculated with allowance for particle porosity, remains nearly constant in the wavelength range where the solar radiation is significant (0.4–2 μm). At the same time its absolute values (both real and imaginary parts) are several times less than the corresponding part of the original constant. The third-level hierarchical aggregates become rather transparent in the interval of sizes 10^{-5} – 10^{-3} m, Q_{PR} monotonically increases from about 0.5 to 0.99 for the dense BAM2³ aggregates, and from 0.1 to 0.6 for the fluffy BA³ aggregates. For a given mass (proportional to N), we compared the Q_{PR} values for the aggregates with the largest cross-section to the cross-section averaged over all simulated aggregates. This factor depends only weakly on the size of the pseudo-monomers: if $R_{\text{eff}} > 10^{-4}$ m, the deviation is

²<http://rredc.nrel.gov/solar/spectra/am0/>

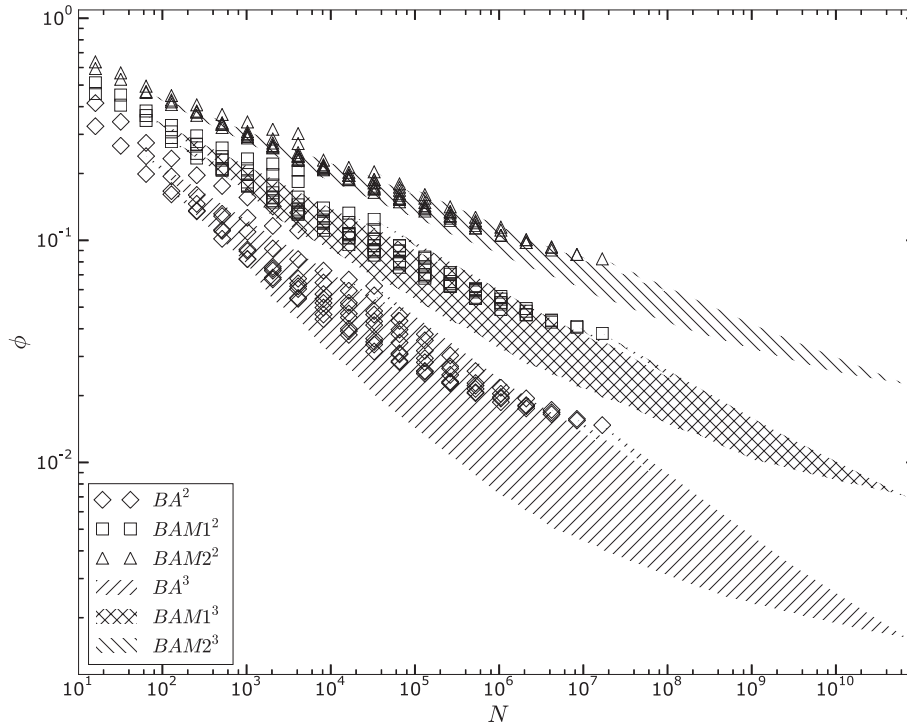


Figure 3. Filling factor for different types of hierarchic aggregates as a function of the number of monomers N (filled area – BA^3 , $BAM1^3$, $BAM2^3$, diamonds – BA^2 , squares – $BAM1^2$, and triangles – $BAM2^2$).

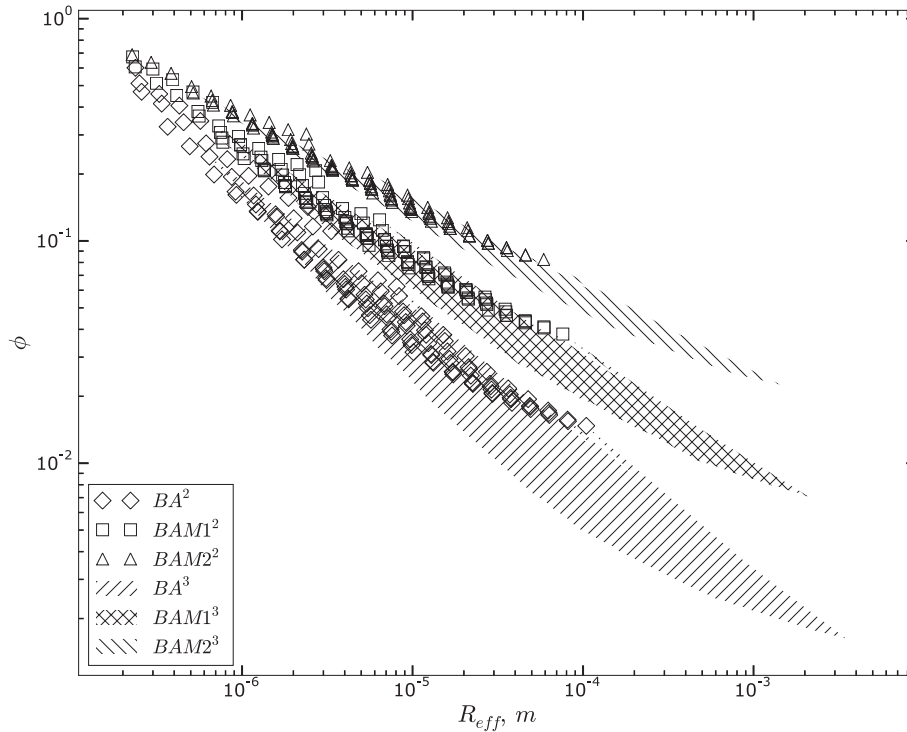


Figure 4. Filling factor for different types of hierarchic aggregates as a function of the effective radius of the aggregates, R_{eff} (filled area – BA^3 , $BAM1^3$, $BAM2^3$, diamonds – BA^2 , squares – $BAM1^2$ and triangles – $BAM2^2$).

less than 10 percent for the BA^3 particles and several times less for the $BAM2^3$ particles. This result allows us to use an average cross-section for aggregates of a given mass.

3.3 Gravity F_{GC} , and centrifugal forces, F_{CF}

Because we are interested in the motion of cometary particles near the nucleus, the solar gravity field is excluded from our considera-

Table 1. Effective aggregate density ρ as a function of particle mass M for hierarchical aggregates of type BA and BAM2.

M , kg	ρ , kg m ⁻³ BA	ρ , kg m ⁻³ BAM2
9.38E-16	837.7	1620.5
1.88E-15	628.2	1463.1
3.75E-15	500.5	1312.0
7.51E-15	392.8	1147.7
1.50E-14	304.0	1014.4
3.00E-14	239.7	901.9
6.01E-14	189.4	799.9
1.20E-13	150.7	712.7
2.40E-13	121.4	637.1
4.80E-13	99.2	570.7
9.61E-13	80.1	507.8
1.92E-12	66.1	453.8
3.84E-12	55.5	408.0
7.69E-12	46.3	366.8
1.54E-11	38.8	329.6
3.07E-11	32.6	296.3
6.15E-11	27.6	266.8
1.23E-10	23.6	240.5
2.46E-10	20.3	217.1
4.92E-10	17.5	196.2
9.84E-10	15.4	178.3
1.97E-09	13.4	162.1
3.94E-09	11.6	146.6
7.87E-09	10.1	132.8
1.57E-08	9.0	120.8
3.15E-08	8.2	110.5
6.30E-08	7.5	101.5
1.26E-07	6.9	93.8
2.52E-07	6.4	87.7
5.04E-07	6.0	82.5
1.01E-06	5.7	78.8

tion. Preserving one-dimensionality and simplicity of our approach we assume that the comet nucleus is a sphere of radius $R_C = 2$ km and mass 10^{13} kg (Pätzold et al. 2016). Here, we try to justify this assumption with a comparison of the gravitational field of a sphere to the field obtained accounting for a realistic shape of 67P/C-G using the digital terrain model (DTM) SHAP5 v1.2 (Preusker et al. 2015), reduced to 200 000 facets. The nucleus is assumed to be homogeneous in both cases, with the density of 533 ± 6 kg m⁻³ (Pätzold et al. 2016). The gravitational acceleration is projected to the normal direction of a corresponding facet in the calculations with the 3D-shaped model. Fig. 5 plots the ratio of the gravitational accelerations of the two models, (g_{3D}/g_{sphere}), for a cometocentric distance of 2 km. It can be clearly seen how the green/blue patches outline the lobes of the body. There are facets that may take negative values, which indicates that the gravitational acceleration is pointing outwards from a facet. Such unusual cases are predominantly located in the concave ‘neck’ region, and correspond to morphological features of cliffs and/or overhangs. We should also point out that in this projection there will be overlaps of values in regions where concavities are present in the DTM. Despite the fact that particles ejected from cliffs and overhangs would suffer a more sophisticated condition of gravity field (typically lower relative to spherical equivalent), the gravity field is on an average ‘quasi-spherical’ with values deviating less than 25–50 per cent from g_{sphere} . In comparison to the different forces, g_{sphere} is used, which can be considered an upper limit over most of the cometary surface. Several implications of this assumption are discussed in more detail in Section 6.

In addition, with the 3D-shaped model we can also evaluate the centrifugal force, F_{CF} , acting on dust grains. The spin period of the comet is taken to be 12.4 h (Keller et al. 2015). In general, accounting for the realistic shape model the direction of this force does not need to coincide with either the direction of the gravitational force or the direction of the gas drag force. This was already noted by Kramer & Noack (2015), who concluded that the rotation of the nucleus cannot be neglected. To illustrate their argument we show the centrifugal acceleration on the surface in Fig. 6, plotted in latitude/longitude and projected to the normal direction of the facet. Facets in yellow are mostly located on facets with low inclination and at large cometocentric distances. The facets with a near-zero acceleration are located around the poles (north and south), or they represent facets with a tilt angle around 90 degrees. Negative values correspond to centrifugal acceleration pointing into the surface, these facets have large surface tilt angles and are mostly located in the concave region in the neck area, and/or overhangs. An important observation is that all the values are about an order of magnitude lower than the acceleration due to gravity (which has a typical value of $\sim 10^{-3}$ ms⁻²). In this work, we choose an inertial coordinate system, nevertheless, we provide an illustration on the magnitude of F_{CF} for our later discussion.

4 COMPARISON OF FORCES

Ratios for various pairs of forces (F_{GD}/F_{GC} , F_{GD}/F_R , and F_R/F_{GC}) as a function of aggregate mass are shown in Fig. 7, at the cometocentric distance of 2 km, and Fig. 8 at 20 km distance. Because the characteristics of BAM1 aggregates always have intermediate values lying between the extreme cases of the BA and BAM2 aggregates we do not plot them for clarity. The gas drag force was evaluated at two limiting cases: continuous F_{GD}^{EF} and free molecular F_{GD}^{FMF} flow. For comparison, the ratio of forces acting on solid silicate spheres of the same mass is given in the figures.

The third-level hierarchical aggregates presented in this work represent millimeter-sized particles with masses of the order of milligrams. Therefore, they are about four orders of magnitude larger in mass than the ones considered in Paper I, and a better representation to the cometary grains detected *in situ* by GIADA (Della Corte et al. 2015; Rotundi et al. 2015). However, despite the significant increase in size and mass of the aggregates, the main conclusions in Paper I remain valid.

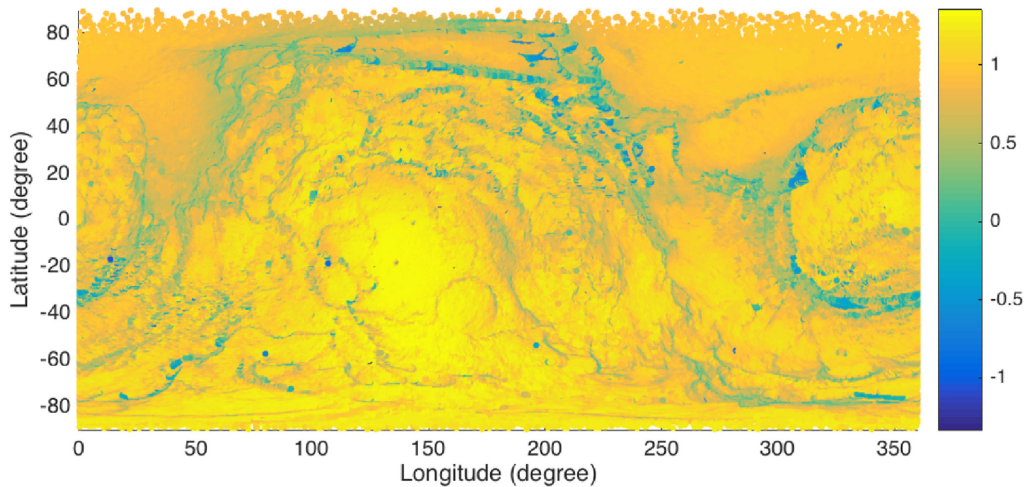
4.1 At 2 km distance

The gas drag force F_{GD} dominates in the vicinity of the nucleus (Fig. 7) for the entire range of tested masses and all particle types (BA, BAM1, and BAM2). The ratio, F_{GD}/F_{GC} , decreases with increasing particle size, ranging from several hundred for picogram grains to less than one for milligram grains. This feature clearly indicates that the modelled structure of the hierarchical aggregates is close to $D_f = 3$. It is also visible that the ratio decreases somewhat slower than for the purely spherical grains.

In Paper I it was assumed that the gas outflow velocity is constant. In such case the ratio, F_{GD}/F_{GC} , is independent of distance to the comet. In this work we used both the EF and FMF models for gas velocity which at first increases with the distance but reaches a nearly constant value at distances of about ten nucleus radii. The gas speed increases approximately two and three times for the FMF and EF models, respectively. Another factor affecting F_{GD} is the noticeable decrease in the drag coefficient (C_D) due to the accelerating gas (via the so-called speed ratio, see equation 3 in

Table 2. Velocity u_i , density ρ_g , and dynamic pressure of gas as a function of the cometocentric distance r for two models: free molecular flow (FMF) and Euler flow (EF).

r, m	$u_i, m s^{-1}$		$\rho_g, kg m^{-3}$		$\rho_g V^2, kg m s^{-2}$	
	FMF	EF	FMF	EF	FMF	EF
2000	429.8	429.8	1.85E-10	1.85E-10	3.42E-05	3.42E-05
2400	667.4	667.6	8.28E-11	8.28E-11	3.69E-05	3.69E-05
2800	730.7	745.7	5.56E-11	5.44E-11	2.97E-05	3.03E-05
3200	765.4	795.9	4.06E-11	3.90E-11	2.38E-05	2.47E-05
3600	787.3	832.0	3.12E-11	2.95E-11	1.93E-05	2.04E-05
4000	802.1	859.7	2.48E-11	2.31E-11	1.60E-05	1.71E-05
4400	812.7	881.8	2.02E-11	1.86E-11	1.34E-05	1.45E-05
4800	820.6	900.0	1.68E-11	1.53E-11	1.13E-05	1.24E-05
5200	826.6	915.2	1.42E-11	1.29E-11	9.73E-06	1.08E-05
5600	831.3	928.2	1.22E-11	1.09E-11	8.44E-06	9.42E-06
6000	835.1	939.5	1.06E-11	9.41E-12	7.38E-06	8.31E-06
6400	838.2	949.4	9.27E-12	8.19E-12	6.51E-06	7.38E-06
6800	840.7	958.1	8.19E-12	7.18E-12	5.79E-06	6.59E-06
7200	842.8	965.9	7.29E-12	6.36E-12	5.17E-06	5.93E-06
7600	844.5	972.9	6.53E-12	5.66E-12	4.65E-06	5.36E-06
8000	846.0	979.3	5.88E-12	5.08E-12	4.21E-06	4.87E-06
8400	847.3	985.1	5.32E-12	4.58E-12	3.82E-06	4.44E-06
8800	848.4	990.3	4.84E-12	4.15E-12	3.49E-06	4.07E-06
9200	849.4	995.2	4.43E-12	3.78E-12	3.19E-06	3.74E-06
9600	850.3	999.6	4.06E-12	3.46E-12	2.94E-06	3.45E-06
10000	851.0	1003.8	3.74E-12	3.17E-12	2.71E-06	3.19E-06

**Figure 5.** Ratio of surface gravitational acceleration of the real 3D-shaped model of comet 67P/CG to a sphere with radius of 2 km and mass of 10^{13} kg on a longitude–latitude map.

Paper I). Simple calculations show that for the FMF approximation this coefficient decreases approximately by half at a distance of five radii. This reduction in C_D almost compensates the relative increase of F_{GD} due to the accelerated expansion. Still, the ratio F_{GD}/F_{GC} is no longer constant, however, the variation with radial distance is not significant.

Interestingly, the radiation pressure, F_R for BA^3 and $BAM2^3$, having different porosities (but the same mass) varies significantly. The ratio F_{GD}/F_R shows three different curves. The hierarchical porous aggregates are more transparent with Q_{PR} smaller than unity for $BAM2$ particles up to hundreds of microns in size, and for BA particles up to millimeters. Therefore, the characteristic value of F_{GD}/F_R is greater than the ratio obtained in Paper I. This effect is clearly manifested when comparing the F_R/F_{GC} curves. In Paper I (using Mie theory) we found that $F_R > F_{GC}$ for the small grains

($M < 10^{-13}$ kg), but $F_R \approx F_{GC}$ for the more massive tested particles ($M = 10^{-10}$ kg). In the current model using EMT, the ratio F_R/F_{GC} is about unity for the smallest particles, about one-tenth for the most massive BA^3 and about two-hundredths for $BAM2^3$.

4.2 At 20 km distance

Outside the zone of the effective gas flow acceleration ($H \lesssim 10$ km) the ratio F_{GD}/F_{GC} does not change relative to the results presented in Paper I. The calculations show that updating the gas flow model (from constant-speed expansion to free molecular flow) leads only to minor changes in the gas drag force. The difference between the EF model and the FMF model is also not significant (<20 per cent in the region of consideration). Since only the radiation pressure does not depend on the cometocentric distance, the role of this

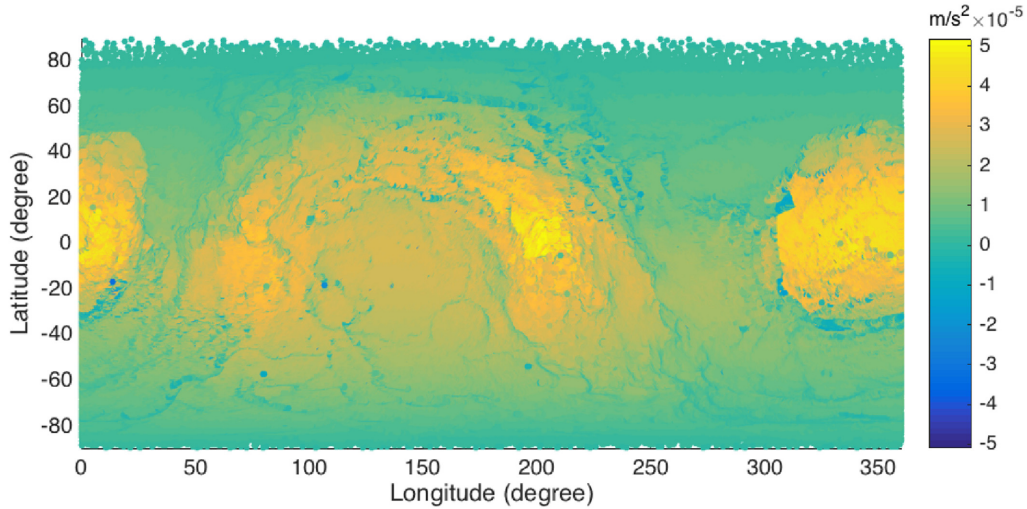


Figure 6. Distribution of centrifugal accelerations on the real 3D-shaped model surface of comet 67P/CG in longitude and latitude coordinates.

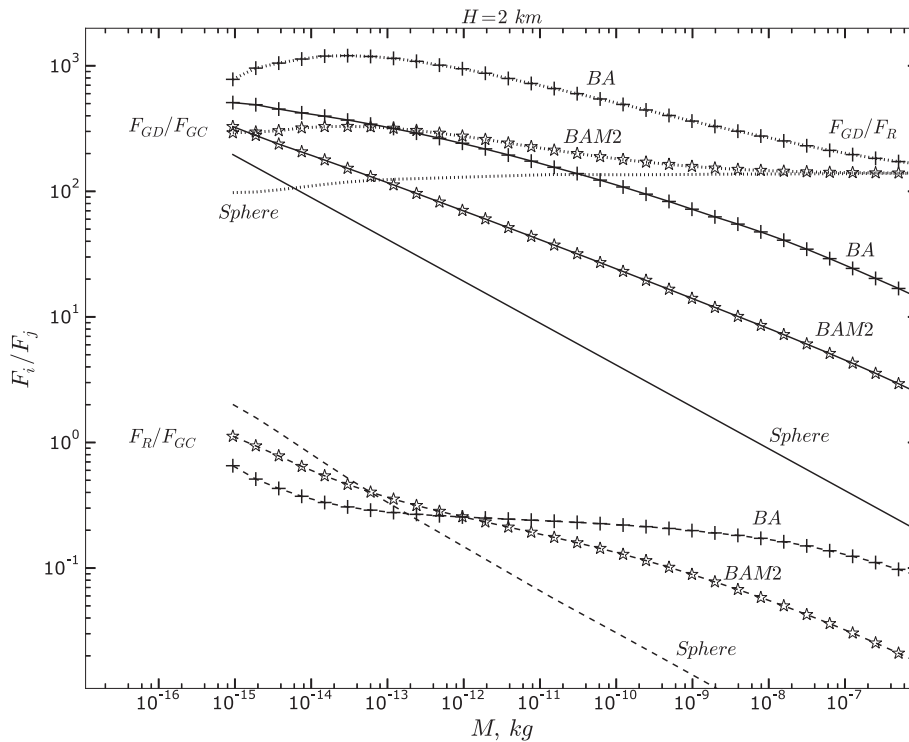


Figure 7. Ratio of forces: F_{GD}/F_{GC} (solid curves), F_{GD}/F_R (dotted curves), and F_R/F_{GC} (dashed curves) as a function of aggregate mass (or number of monomers) at 2 km from the comet centre. Results for BA^3 (crosses) and $BAM2^3$ (stars) aggregates and solid spheres are shown.

force grows rapidly as the distance increases. For the BA^3 particles it exceeds the force of gravity for all tested masses (i.e. up to 10^{-6} kg), for the denser $BAM2^3$ particles it remains larger than F_{GC} up to particle masses of about 10^{-8} kg. The ratio of the gas drag force to the radiation-pressure force depends slightly on the particle mass and is about two for the most massive particles of all types. For the smaller particles this ratio varies from 3–4 ($BAM2^3$) to 10–15 (BA^3).

Thus, one can conclude that in the near-nuclear region ($H < 20$ km) at the considered heliocentric distance $R_H = 3.2$ au and for the assumed total gas production rate of 2 kg s^{-1} , the gas

drag force is dominant for particles with a size of up to several millimeters and the perturbations introduced by other forces are insignificant. However, already in the region of about one hundred kilometers from the nucleus, the account of radiation pressure may be important, mostly as a result of the spherical expansion of the sublimating gas.

5 AGGREGATE SPEEDS IN THE INNER COMA

The calculations of forces presented in the previous section allow us to evaluate the dust speed near the comet nucleus. This is an important issue to consider in connection with the observations

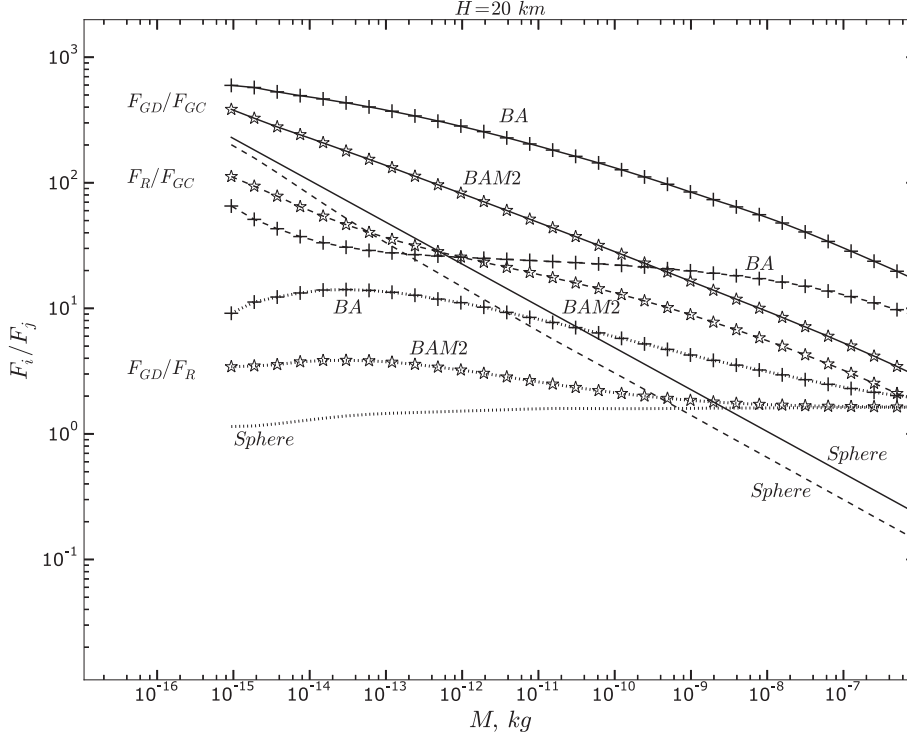


Figure 8. Ratio of forces: F_{GD}/F_{GC} (solid curves), F_{GD}/F_R (dotted curves), and F_R/F_{GC} (dashed curves) as a function of aggregate mass (or number of monomers) at 20 km from the comet centre. Results for BA^3 (crosses) and $BAM2^3$ (stars) aggregates and solid spheres are shown.

by the GIADA instrument on-board Rosetta. It may also play a significant role in the study of particle strength when the collisions among particles (or other targets) are considered, with or without their destruction (Hornung et al. 2016). In this section, we evaluate the velocity for the different types of aggregates (BA^3 and $BAM2^3$) in a wide range of masses ($10^{-15} < M < 10^{-6}$ kg). The velocities are numerically calculated solving the equation of motion,

$$\ddot{r} = G \frac{M_C}{r^2} + \frac{1}{2} C_D \frac{A}{m} n_l m_{H_2O} (u_l - v_d)^2 \pm \frac{F_R}{m}, \quad (3)$$

where G is the gravity constant, M_C , the comet nucleus mass, F_R the radiation pressure at the heliocentric distance 3.2 au. In order to preserve the one-dimensionality of the model, we consider only the dust motion in the directions to and from the Sun (the solar and anti-solar directions).

The relative difference between the drag forces calculated in the frame of the EF and FMF methods is less than 25 per cent in the considered region ($H < 20$ km). At the same time both these methodologies produce a drag force greater than that of the model with a constant-speed expansion, and this difference grows monotonically with distance (15 per cent for the FMF model and about 40 per cent for the EF model at $H = 20$ km).

In Fig. 9 the dust velocity as a function of particle mass M at 10 km from the cometary centre is shown when the dust is accelerated only by gas drag and the nucleus gravity (F_R is ignored). The results of the two models of gas expansions (EF and FMF) were examined for each type of aggregate, but one can see that the velocity difference does not exceed 5 per cent over the entire mass range. Therefore in the subsequent figures we present the results obtained with the FMF method only.

A comparison to the velocity of a solid sphere of the same mass is shown in Fig. 9. In this case the effect of gravity is clearly visible for large particles: the velocity curve bends downward and the slope

(dV/dM) increases. For porous aggregates the drag force exceeds the force of gravity in the considered region by many times (see Figs. 9, 10). As a result, the relative deceleration of the dust due to the nucleus gravity is negligible: the slope of the curves noticeably changes only for the most massive particles.

Results obtained at a cometocentric distance of 30 km are very close to the previous ones. Our conclusion based on the analysis of forces is completely confirmed by the calculations: in the considered model all aggregates get the final constant expansion speed during the first ten kilometres above the nucleus surface.

At the final stage we add into consideration a radiation pressure acting on the dust. Because we apply a 1D model, this model extension is intended to show only qualitatively the influence of radiation pressure on the particle dynamics. The motion of particles started from the sub-solar point (where radiation force and comet gravity are opposite to gas drag force) and the anti-solar point (where radiation force and gas drag force are opposite to comet gravity) is calculated. The latter case is only an illustrative one, because the nucleus shadow is not considered. In Fig. 10 we show the simulation results when all major forces (F_{GD} , F_{GC} , F_R) act on the BA and BAM2 model aggregates. Results for solid spheres are also plotted in the figure. The cometocentric distance is 30 km. This distance approximately corresponds to positions where the particle velocities were detected by GIADA (Della Corte et al. 2015). As before the drag force F_{GD} is calculated for the FMF gas expansion model and the radiation-pressure force F_R is calculated based on the combination of the Mie theory and the EMT. We note that the radiation pressure does not make any appreciable contribution for the considered distances. For the porous model aggregates the velocities of particles that are started at opposite points (sub-solar and anti-solar) are practically indistinguishable at 8 km above the surface. At 30 km the difference is detectable, but still very small. Thus, the

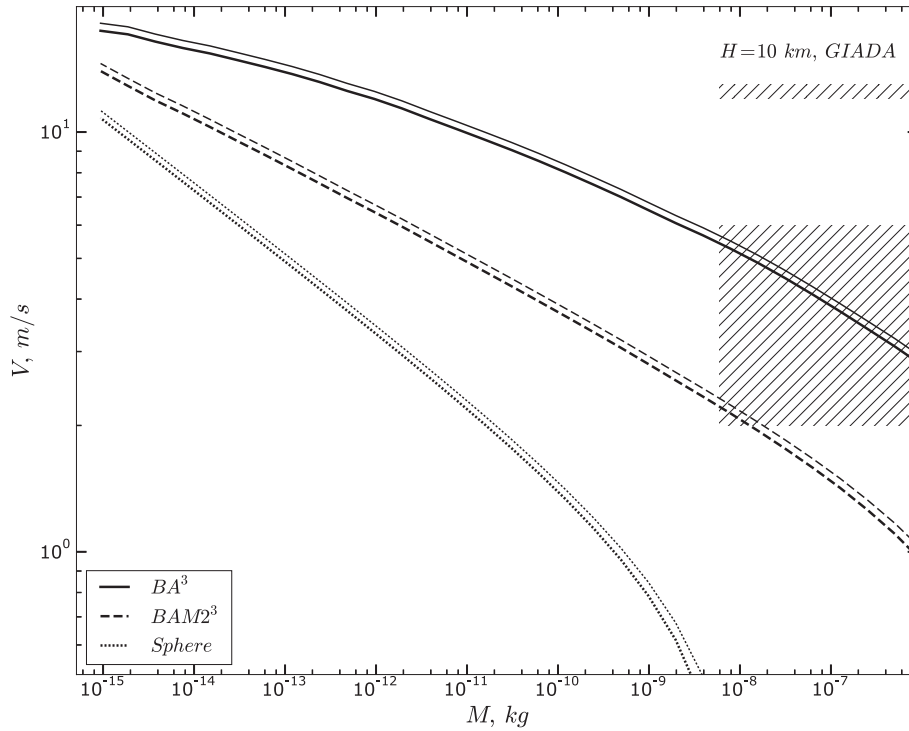


Figure 9. Velocity of hierarchic aggregates as a function of aggregate mass at 10 km from the centre of the nucleus. In the equation of motion only the drag force and gravity were used. An EF is shown with thin lines and an FMF with thick lines. The GIADA detectability ranges are indicated as filled area.

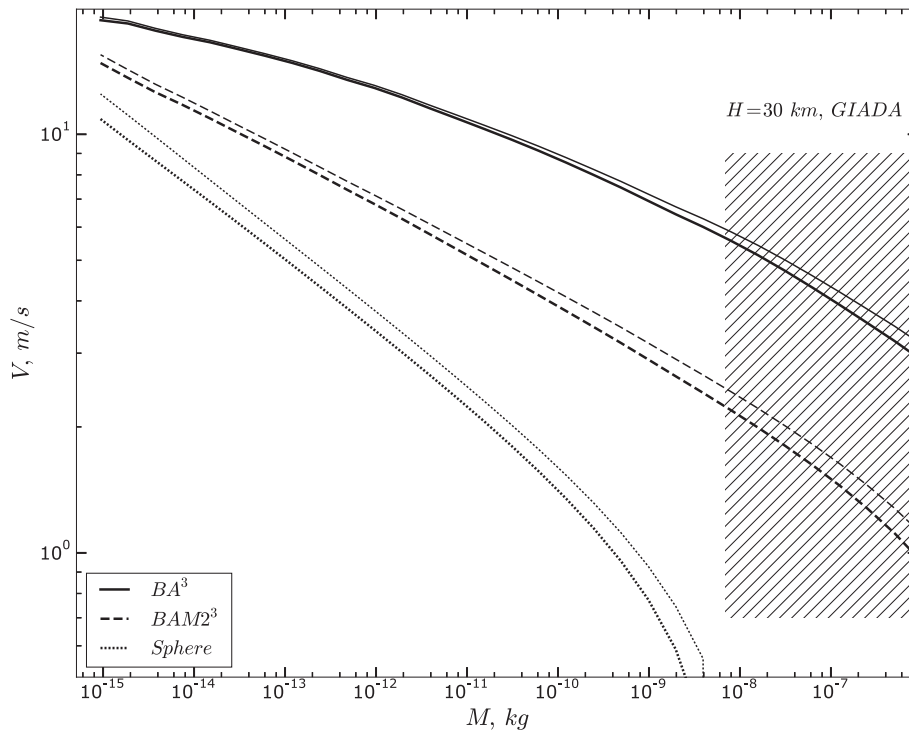


Figure 10. Velocity of hierarchic aggregate as a function of aggregate mass at 30 km from the centre of the nucleus. The equation of motion contains drag force, gravity, and radiation pressure. The range of possible values for the same aggregate mass stems from the orientation-dependent radiation force and is shown as double curves. The GIADA detectability ranges are indicated as filled area.

conclusion made above can be strengthened: in the vicinity of the cometary nucleus (<30 km), it is possible with sufficient accuracy to calculate the velocity of a dust particle with a mass up to about

one milligram on the basis of the model taking into account only the gas drag force. It is clear from our calculations that it is the porous aggregates that have velocities comparable with observed

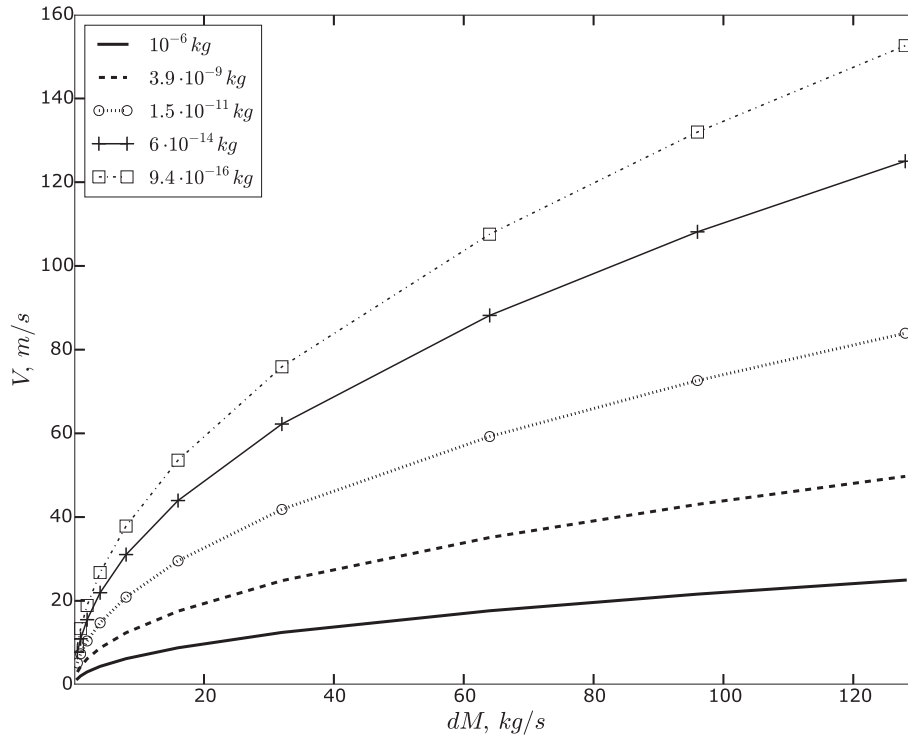


Figure 11. Velocity of hierarchic aggregate BA^3 as a function of total gas production dM at 30 km from the centre of the nucleus. The different curves assume different mass of the aggregate (see text for details).

velocities, considering the imperfect knowledge of the main characteristics of dust particles (shape, size, effective density, etc.). We should also note that the smallest density of our model particles is about 5 kg m^{-3} , whereas Fulle et al. (2015) report bulk particle density about 1 kg m^{-3} , which is still a non-negligible difference.

The dust velocities given in this work were calculated for a production rates of 2 kg s^{-1} , in order to make a qualitative comparison with the Rosetta results (see Figs 9–10). However, we can estimate the dust velocity for higher total gas productions, with an expectation that they should be correlated. Although in general, this dependence has a non-linear character. The results of the simulation are given in Fig. 11, showing velocities of BA^3 aggregates versus gas production rate. Only the gas drag force and the gravity of the nucleus are considered in these calculations, neglecting the radiation pressure. The different curves correspond to velocities for aggregates with different masses, covering the entire model range.

It should be noted that although the generated aggregates under consideration is statistically spherically symmetric, they are not ideal spheres (as was stressed in Shen et al. 2008). Thus, an effective cross-section of the considered aggregates is not circular. In general, asymmetric particles being set in expanding gas flow, are not only accelerated but also rotated by the gas. This effect leads to a partial dissipation of translational energy and to a relative loss of acceleration. Ivanovski et al. (2017a,b) considered the role of this effect and computed its influence on the terminal velocities, however, for particles of significantly larger mass than considered here. Unfortunately, there is no information from Rosetta on the rotational state of these small particles, hence, a possible attempt to rigorously model this effects remains completely academic, and we do not consider this effect in this paper.

6 SUMMARY

In this paper, we analysed the major forces acting on realistically modelled, large, and extremely fluffy dust particles, out to distances of 20 cometary radii. We tried to understand how the motion of dust of different sizes and masses is governed when the internal porous texture is modified. This work is a direct extension of the model presented in Paper I, however, improving on a number of previous simplifying assumptions and methodologies, which leads to new insights and modification of the earlier results.

The new model developments allowed us to construct hierarchical aggregates of the third level. We showed that the characteristics of hierarchical aggregates of a given type change significantly when the sizes of the constituent sub-blocks (i.e. aggregates of a lower level) change. The effective density of a fixed-mass model particle may vary over a wide range and it is no longer a unique characteristic of the aggregate type. Also, the basic properties of these particles differ from the properties of the classical porous ballistic aggregates, that are widely used in cometary physics. However, for a more accurate modelling we conclude that future observations/analyses of available Rosetta data should try to determine the properties of grains, their chemical composition, porosity, and shape.

The dynamical properties of the newly constructed particles were examined from relative contribution of (1) the acceleration due to gravity of the cometary nucleus, (2) the solar radiation pressure, and (3) the acceleration of dust particles by the gas flow. Although all the calculations were performed for a spherical homogeneous nucleus, we also presented qualitative estimates for the gravity force of nucleus and centrifugal force obtained for a real 3D-shaped model. The most severe discrepancies between fields using the 3D and spherical shape are in areas with a considerable number of cliffs, overhangs, and concavities (the ‘neck’ region). The dust grains emanating from these areas may be expected to have likely higher

velocities than those derived from the spherical nucleus. The effect of the real gravitational field and the three-dimensional gas flow on the acceleration of dust particles will be considered in the future paper, using a 3D DSMC model (Marschall et al. 2017, 2016; Liao et al. 2016).

The radiation pressure calculations were updated using the effective medium theory method with the Maxwell–Garnett mixing rule, which significantly alters the results relative to the commonly used Mie theory. The scattering efficiency of the dust particles due to the porosity changes (e.g. BA versus BAM2) is more pronounced than the corresponding variation due to the change of the aggregate size (as observed in the Mie model), that is, the scattering characteristics of the BA and BAM2 particles of the same mass can differ by hundreds of per cent. And even though the radiation pressure plays an important role only at larger distances from the nucleus it appears that there are conditions, depending on the illumination geometry, where dust can become ‘stagnant’ or reverse its direction of motion due to F_R effects. This effect should be studied in detail using the 3D shaped model, but there is at least some observational evidence of a small fraction of dust grains moving towards the nucleus (Güttler et al. 2017).

At last we also considered two limiting cases of gas expansion, an EF and a FMF. For all considered particle types and sizes the dust is effectively accelerated in the region within 10 nucleus radii for both types of flow. Relying on a non-constant gas acceleration also leads to a decrease in the velocity for all the particle types of all masses considered. Thus, we conclude that this effect is important for the quantitative evaluation of the dust velocity in the nearest coma. The velocities calculated for all types of hierarchical aggregates considered in the paper agree qualitatively with measured ones from GIADA. It also means that we cannot yet choose a preferred type of the ballistic particle–cluster aggregation based on these data.

ACKNOWLEDGEMENTS

Yu.S. and V.R. wish to express their gratitude to the International Space Science Institute (ISSI) at Bern for support of their collaboration in the framework of the Visiting Science Program. Yu.S. thanks the Deutsche Forschungsgemeinschaft (DFG) for support under grant SK 264/2–1. Y.H. Zhao thanks the support from the National Natural Science Foundation of China (grant No: 11673072, 11761131008). L.R. was in part supported by the Deutsche Forschungsgemeinschaft (DFG) project: 392267849.

REFERENCES

- Bentley M. S. et al., 2016, *Nature*, 537, 73
 Bohren C. F., Huffman D. R., 1983, *Absorption and Scattering of Light by Small Particles*. John Wiley and Sons, New York
 Della Corte V. et al., 2015, *A&A*, 583, A13
 Dominik C., 2009, in Henning Thomas, Grün Eberhard, Steinacker Jürgen, eds, *ASP Conf. Ser.*, 414, San Francisco, p. 494
 Fulle M. et al., 2015, *ApJ*, 802, L12
 Fulle M. et al., 2016, *ApJ*, 821, 19
 Fulle M. et al., 2017, *MNRAS*, 469, S45
 Güttler C. et al., 2017, *MNRAS*, 469, S312
 Hornung K. et al., 2016, *Planet. Space Sci.*, 133, 63
 Ivanovski S. L. et al., 2017a, *MNRAS*, 469, S774
 Ivanovski S. L., Zakharov V. V., Della Corte V., Crifo J.-F., Rotundi A., Fulle M., 2017b, *Icarus*, 282, 333
 Keller H. U. et al., 2015, *A&A*, 583, A34
 Kissel J. et al., 1986, *Nature*, 321, 336
 Köhler M., Minato T., Kimura H., Mann I., 2007, *Adv. Space Res.*, 40, 266
 Kozasa T., Blum J., Mukai T., 1992, *A&A*, 263, 423
 Kramer T., Noack M., 2015, *ApJ*, 813, L33
 Langevin Y. et al., 2016, *Icarus*, 271, 76
 Laor A., Draine B. T., 1993, *ApJ*, 402, 441
 Li A., Draine B. T., 2001, *ApJ*, 554, 778
 Liao Y. et al., 2016, *Earth Moon Planets*, 117, 41
 Mannel T., Bentley M. S., Schmied R., Jeszenszky H., Lvasseur-Regourd A. C., Romstedt J., Torkar K., 2016, *MNRAS*, 462, S304
 Marschall R. et al., 2016, *A&A*, 589, A90
 Marschall R. et al., 2017, *A&A*, 605, A112
 Merouane S. et al., 2016, *A&A*, 596, A87
 Minato T., Köhler M., Kimura H., Mann I., Yamamoto T., 2006, *A&A*, 452, 701
 Mukai T., Ishimoto H., Kozasa T., Blum J., Greenberg J. M., 1992, *A&A*, 262, 315
 Nakamura R., Kitada Y., Mukai T., 1994, *Planet. Space Sci.*, 42, 721
 Okuzumi S., Tanaka H., Sakagami M.-A., 2009, *ApJ*, 707, 1247
 Ott T. et al., 2017, *MNRAS*, 469, S276
 Pätzold M. et al., 2016, *Nature*, 530, 63
 Preusker F. et al., 2015, *A&A*, 583, A33
 Rotundi A. et al., 2015, *Science*, 347, 3905,
 Schulz R. et al., 2015, *Nature*, 518, 216
 Shen Y., Draine B. T., Johnson E. T., 2008, *ApJ*, 689, 260
 Skorov Yu., Reshetnyk V., Lacerda P., Hartogh P., Blum J., 2016, *MNRAS*, 461, 3410
 Sone Y., Sugimoto H., 1993, *Phys. Fluids*, 5, 1491

This paper has been typeset from a $\text{\TeX}/\text{\LaTeX}$ file prepared by the author.